Efficiency and survivability analysis of a point-absorber wave energy converter using DualSPHysics

Pablo Ropero-Giralda[1], Alejandro J. C. Crespo[1], Bonaventura Tagliafierro[2], Corrado Altomare[3,4], José M. Domínguez[1], Moncho Gómez-Gesteira[1], Giacomo Viccione[2]

[1] Universidade de Vigo, CIM-Uvigo, Ourense, Spain

[2] Università degli Studi di Salerno, Fisciano, Italy

[3] Universitat Politècnica de Catalunya, Barcelona, Spain

[4] Universiteit Gent, Ghent, Belgium

Abstract

Smoothed Particle Hydrodynamics (SPH) method is used here to simulate a heaving point-absorber with a Power Take-Off system (PTO). The SPH-based code DualSPHysics is first validated with experimental data of regular waves interacting with the point-absorber. Comparison between the numerical and experimental heave displacement and velocity of the device show a good agreement for a given regular wave condition and different configurations of the PTO system. The validated numerical tool is then employed to investigate the efficiency of the proposed system. The efficiency, which is defined here as the ratio between the power absorbed by the point-absorber and its theoretical maximum, is obtained for different wave conditions and several arrangements of the PTO system. Finally, the effects of highly energetic sea states on the buoy are examined through alternative configurations of the initial system. A survivability study is carried out by computing the horizontal and vertical forces exerted by focused waves on the wave energy converter (WEC). The yield criterion is used to determine that submerging the heaving buoy at a certain depth is the most effective strategy to reduce the loads acting on the WEC and its structure, while keeping the WEC floating at still water level is the worst-case scenario.

Keywords: point-absorber, WEC, survivability, efficiency, CFD, SPH

1. Introduction

Wave energy is nowadays recognised as one of the renewable energy resources with the highest potential, availability, and predictability (Chongwei et al., 2014). However, the wave energy potential is still not fully exploited. Despite the efforts of the scientific community (Bozzi et al., 2018, Kamranzad and Hadadpour, 2020), an agreement about the proper type of Wave Energy Converters (WECs) has not been achieved yet. The wave devices are, in most cases, placed offshore, where wave energy potential is higher but where they are subjected to great forces. Eventual rogue waves arising from a random sea state are potentially dangerous for the device and need to be correctly characterised. This may be accomplished by means of single events with a specific crest height and an associated period, known as focused waves. Therefore, the WEC design needs to be based not only on the efficiency but also on the survivability of the devices, which is key to harness wave energy in a safe and cost-effective way. Many ingenious systems have been developed but only a few are generating electricity commercially (Drew et al., 2009). One of the most widespread devices are the point-absorbers, which typically consist of a floater whose oscillating motion, heaving and/or pitching, is converted into electricity by means of a Power Take-Off (PTO) system (Ahamed et al., 2020). They are non-directional devices that can absorb energy from all directions through their movement at/near the water surface. Their simplicity makes point-absorbers more resilient to extreme wave conditions than other wave energy devices.

Numerical modelling plays a fundamental role as a complementary tool for physical experiments during the design stage of WECs. It has become a game-changer in the wave energy industry thanks to the exponential growth of the computational resources, which makes possible to simulate large and complex systems at

reasonable computational runtime (Folley, 2016). On one hand, numerical methods allow reducing costs and time when different configurations need to be evaluated. The data obtained from the simulations can be of great help to determine design loads, stresses, or any other meaningful information, which is hard or even impossible to evaluate during physical tests. On the other hand, numerical models purposely developed for efficiency analysis of WECs may not be appropriate to evaluate their survivability. The numerical model should be able to solve the interaction between incoming waves and floating structures, and to reproduce the behaviour of the PTO systems in an accurate way. Several modelling approaches have been employed to analyse the hydrodynamic response of WECs as shown in the following review papers: Li and Yu (2012); Folley et al. (2012); Markel and Ringwood (2016); Penalba et al. (2017); Zabala et al. (2019); Davidson and Costello (2020). However, only a few numerical pieces of research include the mechanical constraints of the PTO system.

Traditionally, the most widely used models to describe the response of a WEC under operational sea states are based on potential flow theory (see e.g., Newman, 2018). They are either time or frequency domain models that apply the boundary element method (BEM) to solve the frequency-dependent dynamics of the device. Many works have assessed the performance of point-absorbers using potential flow theory, e.g. Beatty et al. (2015), De Andrés et al. (2013), and Rahmati and Aggilis (2016). Nevertheless, potential flow-based codes, such as WAMIT (Lee, 1995) or NEMOH (Babarit and Delhommeau, 2015), assume the fluid to be incompressible, inviscid and irrotational, the motion of the device to have small amplitude, and the waves to be linear. These assumptions are likely to be violated when a WEC is placed at sea, especially under energetic sea states. Conversely, CFD (Computational Fluid Dynamics) methods are more time consuming and complex, but they do not require any of the previous simplifications. They are based on the Navier-Stokes equations, which may be solved following an Eulerian approach (mesh-based methods) or a Lagrangian approach (mesh-free methods). The mesh-based methods have proved to be very robust since they have been developed for many years. In particular, the finite volume method has been applied to a wide range of free-surface problems providing accurate results. Power efficiency analysis of point-absorbers using these methods have been conducted by Yu and Li (2013), Jin et al. (2018), and Reabroy et al. (2019), amongst others. The interaction of focused waves with vertical cylinders has been studied by Westphalen et al. (2012) and Hu et al. (2016) using the mesh-based codes STAR-CCM+ and OpenFOAM, respectively. Nevertheless, defining an appropriate mesh can be very inefficient for complex systems with moving boundaries. On the other hand, meshless methods can be applied to highly nonlinear problems with arbitrary and changing geometries, difficult to handle with mesh-based methods.

Different meshless approaches have been developed in the last decades. One of the most popular methods is the Smoothed Particle Hydrodynamics (SPH), which has reached the required maturity level to be used for engineering purposes (Violeau and Rogers, 2016). The continuum fluid in SPH is treated as discrete *smoothed* quantities at locations named *particles*. The physical quantities are computed at each *particle* as an interpolation of the quantities of the surrounding particles using a weighted function (kernel) based on the distance between particles and solving the Navier-Stokes equations. The SPH technique presents several advantages over mesh-based methods to simulate free-surface flows since there is no special detection of that free surface. Large deformations can be efficiently treated (there is no mesh distortion), and violent impacts of extreme waves with fixed or fluid-driven objects can be easily tackled. In addition, rapidly moving complex geometries are handled with SPH in a straightforward way, without problems related to mesh generation or updating at each time step. There are several papers that show the robustness of SPH for coastal engineering applications, such as Gotoh and Khayyer (2018), Khayyer et al. (2018), and González-Cao et al. (2018). With a focus on the WEC modelling, the pioneering works of Rafiee et al. (2013) and Edge et al. (2014) presented the SPH simulation of oscillating wave surge devices. Westphalen et al. (2014) compared the hydrodynamic response of a point-absorber obtained with SPH and with a finite volume method, whilst Omidvar et al. (2013) and Yeylaghi et al. (2015) are the first works to deal with the interaction between extreme waves and point-absorbers using SPH methods.

Among the different SPH codes, DualSPHysics software is considered one of the most efficient SPH solvers (Crespo et al., 2015). DualSPHysics is open-source (www.dual.sphysics.org) and allows applying the SPH method to real engineering problems. It can be executed not only on CPUs, but also on GPU (Graphics

Processing Unit) cards with powerful parallel computing that can be installed in a personal computer (Altomare et al., 2018). The DualSPHysics code has been applied in this work since it includes the coupling with the open-source multiphysics platform Project Chrono (Tasora et al., 2016), which is capable of simulating collisions and kinematic restrictions such as springs, hinges, pulleys, etc. In this manner, the coupling of DualSPHysics with Project Chrono allows the complex mechanisms of the PTO system to be reproduced within the same meshless framework. DualSPHysics has proven its capability to generate and propagate waves (Altomare et al., 2017; Domínguez et al., 2019a) and to simulate satisfactorily their interaction with WECs such as an Oscillating Water Column in Crespo et al. (2017, 2018) and an Oscillating Wave Surge Converter in Brito et al. (2020). The first work where DualSPHysics was employed to simulate a point-absorber device was presented in Tagliafierro et al. (2019). Other works, like Verbrugghe et al. (2018, 2019), combined the capabilities of a fully nonlinear potential flow solver and DualSPHysics, allowing the simulation of large domains and, at the same time, accurate and detailed modelling of the interactions between waves and the WEC.

This research is focused on the simulation of a wave energy converter consisting of a cylindrical heaving-buoy attached to a PTO system, as described by Zang et al. (2018), who conducted experiments with a model scale of 1:10. The PTO system is a direct-drive linear generator in which the rod connected to the buoy moves the alternator in the presence of a stationary magnetic field, inducing an electric current in the stator, according to Faraday's law of induction (Eriksson et al., 2005). The present manuscript includes a complete numerical study in terms of SPH modelling of a point-absorber converter since it contains: i) validation with experiments, ii) efficiency analysis and iii) survivability under extreme waves. This work is organised as follows: Section 1 is the introductory part and provides the state-of-the-art, Section 2 describes the DualSPHysics code, Section 3 shows the validation comparing numerical results with experimental data using one regular wave condition, Section 4 includes an efficiency study simulating several conditions of regular waves, Section 5 presents the loads exerted onto the point-absorber under the action of focused waves considering different scenarios and, finally, conclusions are synthesised in Section 6.

2. Numerical model

The fundamental concept in the SPH methodology is to discretise the fluid into a set of particles, where the physical quantities (position, velocity, density, and pressure) are obtained as an interpolation of the corresponding quantities of the surrounding particles. The weighted contribution of those particles is obtained using a kernel function (W_{ab}) with an area of influence that is defined using a characteristic *smoothing length* (h). The quintic Wendland kernel (Wendland, 1995) is used in DualSPHysics and it is defined to vanish beyond $2h$. Note that particles are initially created with an interparticle distance, dp, which is used as a reference value to define the smoothing length using $h=2dp$.

The Navier-Stokes equations can be then written in a discrete SPH formalism using W_{ab} as the kernel function, which depends on the normalised distance between particle a and neighbouring b particles

$$\frac{d\boldsymbol{r}_a}{dt} = \boldsymbol{v}_a \tag{1}$$

$$\frac{d\boldsymbol{v}_a}{dt} = -\sum_b m_b \left(\frac{p_b + p_a}{\rho_b \cdot \rho_a} + \Pi_{ab}\right) \nabla_a W_{ab} + \boldsymbol{g} \tag{2}$$

$$\frac{d\rho_a}{dt} = \sum_b m_b \boldsymbol{v}_{ab} \nabla_a W_{ab} + 2\delta hc \sum_b (\rho_b - \rho_a) \frac{\boldsymbol{v}_{ab} \nabla_a W_{ab}}{\boldsymbol{r}_{ab}^2} \frac{m_b}{\rho_b} \tag{3}$$

where t is the time, $\boldsymbol{r}$ is the position, $\boldsymbol{v}$ is the velocity, p is the pressure, ρ is the density, m is the mass, c is the numerical speed of sound, and $\boldsymbol{g}$ is the gravitational acceleration. The artificial viscosity (Π_{ab}) proposed in Monaghan (1992) and the density diffusion term proposed by Fourtakas et al. (2020) (using δ=1) are applied here.

The previous equations allow computing the position, velocity, and density of each SPH particle. However, a new equation to compute pressure is required. In the DualSPHysics code, the fluid is treated as weakly compressible (WCSPH), so that an equation of state is used to calculate fluid pressure as a function of density, rather than solving a Poisson-like equation. Hence the system is closed by using the polytropic equation, Eq. (4), where the speed of sound has been adjusted to obtain a reasonable time step:

$$p = \frac{c^2 \rho_0}{\gamma}\left[\left(\frac{\rho}{\rho_0}\right)^{\gamma} - 1\right] \tag{4}$$

with γ=7 the polytropic constant (Ma, 2010), and ρ_0=1000 kg m^{-3}, the reference density of the fluid.

One of the most interesting capabilities of SPH models is the simulation of fluid-driven objects (Canelas et al., 2015). First, the net force on each individual particle of a floating object is computed as the summation of the contributions of all surrounding fluid particles (b). In this way, each floating particle q experiences a force per unit of mass $\boldsymbol{f_q}$ given by:

$$\boldsymbol{f}_q = \frac{d\boldsymbol{v}_q}{dt} = \sum_{b \in fluid} \frac{d\boldsymbol{v}_{qb}}{dt} \tag{5}$$

where the interactions between particles q and b are solved according to Eq. (2).

It is important to note that here the object is being considered as rigid, so the basic equations of rigid body dynamics are solved to obtain the motion of the floating object:

$$M\frac{d\boldsymbol{V}}{dt} = \sum_{q \in body} m_q \boldsymbol{f}_q \tag{6}$$

$$I\frac{d\boldsymbol{\Omega}}{dt} = \sum_{q \in body} m_q\left(\boldsymbol{r}_q - \boldsymbol{R}\right) \times \boldsymbol{f}_q \tag{7}$$

where M is the total mass of the object, I the moment of inertia, $\boldsymbol{V}$ the velocity, $\boldsymbol{\Omega}$ the rotational velocity, $\boldsymbol{R}$ the centre of mass, and $\boldsymbol{m}_q$ and $\boldsymbol{r}_q$ are, respectively, the mass and position of each floating particle q. Equations (6) and (7) are integrated in time in order to obtain the values of $\boldsymbol{V}$ and $\boldsymbol{\Omega}$ at the beginning of the next time step. Each particle that belongs to the object moves according to the velocity, $\boldsymbol{v}_q$, given by:

$$\boldsymbol{v}_q = \boldsymbol{V} + \boldsymbol{\Omega} \times \left(\boldsymbol{r}_q - \boldsymbol{R}\right) \tag{8}$$

The accuracy of DualSPHysics to simulate fluid-driven objects under the action of regular waves was studied in Domínguez et al. (2019b), where the numerical results of nonlinear waves interacting with a freely floating box were compared with the experimental data from Ren et al. (2015). A good agreement was obtained for the motions of the box in terms of heave, surge, and pitch time series.

The capabilities of DualSPHysics are extended, thanks to the coupling with the multiphysics library Project Chrono (https://projectchrono.org/) that allows solving mechanical constrains applied on rigid bodies during the fluid-structure interaction. Among the different features that can be defined, springs and dampers are straightforward. A more complete description of the coupling between DualSPHysics and Chrono is presented in Canelas et al. (2018), which also provides validation of the features as implemented into the new framework.

The coupled DualSPHysics-Chrono code is employed in this work to simulate a heaving point-absorber whose PTO system is modelled as a linear damper:

$$F_{PTO}(t) = b_{PTO} \cdot v_z(t) \tag{9}$$

where F_{PTO} represents the force exerted by the PTO system, b_{PTO} its damping coefficient and v_z the heave velocity.

3. Validation

The WEC under study is the point-absorber described in Zang et al. (2018). It is composed of a heaving buoy connected to a PTO system at its bottom. More specifically, the PTO system is a direct-drive linear generator, whose effects on the dynamics of the WEC were simulated in the experimental campaign thanks to various air-dampers (Zang et al., 2018) while, mathematically, they can be modelled simply as a linear damper (Eriksson et al., 2005), as shown in Eq. (9). The heaving buoy is a cylinder 0.22 m high with a diameter (D) of 0.50 m and density 500 kg/m^3, which results in a mass of 21.6 kg. Therefore, the draft of the buoy at equilibrium is half its height (0.11 m).

Zang et al. (2018) conducted several experiments to study the response of the WEC under regular waves for different values of the damping coefficient b_{PTO} (Eq. 9). The physical tests conducted with regular waves of wave height H=0.16 m, period T=1.5 s, water depth d=1.10 m, and an associated wavelength L=3.40 m are considered here to validate the numerical code. Three values of the damping coefficient, b_{PTO}=0, 240, 1100 Ns/m, are used in the validation to take the effect of the PTO into account.

A numerical tank (Fig. 1) is designed to mimic the physical flume. The width of the numerical domain is reduced to twice the buoy diameter ($2D$), lateral periodic boundary conditions are applied to minimise the effects of radiated waves from the lateral walls. A piston, whose movement generates the desired wave, is located on the left of the tank (as seen in Fig. 1). The buoy is located at one wavelength (L) from the piston. Wave dissipation is guaranteed on the right side of the tank (Fig. 1) thanks to the combination of a dissipative beach with a slope of α=1:2, starting at L/4 from the buoy, and a numerical damping applied along the longitudinal axis (x) of the beach.

The numerical damping system consists in gradually reducing the velocity of the fluid particles at each time step according to their location, as suggested in Altomare et al. (2017). In this manner, the velocity of a fluid particle a located within the damping zone is reduced from its initial velocity $\boldsymbol{v}_{a,0}$ to its final velocity $\boldsymbol{v}_a$ according to $f_r(x_a,\Delta t)$:

$$\boldsymbol{v}_a = \boldsymbol{v}_{a,0} \cdot f_r(x_a, \Delta t) \tag{10}$$

where x_a is the longitudinal position of the particle, Δt is the duration of the last time step and $f_r(x_a,\Delta t)$ is the reduction function, which employs a quadratic decay:

$$f_r(x_a, \Delta t) = 1 - \Delta t \cdot \beta \cdot \left(\frac{x_a - x_0}{x_1 - x_0}\right)^2 \tag{11}$$

being x_0 and x_1 the initial and final position of the damping zone along the x-axis, respectively, and β a coefficient that is fixed at β = 10 for all simulations.

The overall absorption capabilities of the beach with numerical damping are quantified by means of the reflection coefficient, K_R, which is calculated here using the Healy method (Eagleson and Dean, 1966):

$$K_R = \frac{H_{max} - H_{min}}{H_{max} + H_{min}} \tag{12}$$

where H_{max} and H_{min} are, respectively, the maximum and minimum numerical wave height. In this way, the reflection coefficient of the numerical tank shown in Fig. 1, for the regular wave previously described, is lower than 2%, which means that over 98% of the incident wave energy is being dissipated.

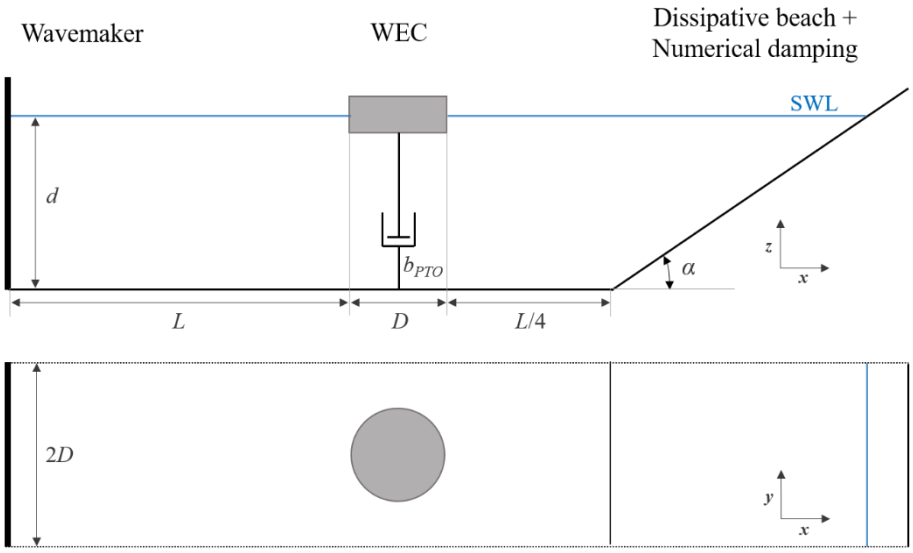

Fig. 1. Numerical tank to simulate the interaction of the WEC under regular waves.

The resolution is given by the initial interparticle distance *dp,* which is employed to create the particles involved in the simulation. Altomare et al. (2017) and Rota-Roselli et al. (2018) proved that using around ten particles per wave height (H/dp=10) provides a reasonable compromise between accuracy and computational time. In this validation, two different resolutions are employed: dp=0.02 m and dp=0.01 m corresponding to H/dp=8 and H/dp=16, respectively. The total number of particles is approximately 800,000 for the simulations with dp=0.02 m, and 6,500,000 with finer resolution dp=0.01 m, as presented in Table 1. The table also shows the computational time required to simulate fifteen seconds of physical time using a GeForce RTX 2080 Ti GPU card. It can be observed that the lower the dp, the higher the number of particles and, therefore, longer runtimes are needed.

Table 1. Number of particles and GPU runtimes (GeForce RTX 2080 Ti).

b_{PTO} [Ns/m]	dp [m]	Particles	Runtime [h]
0	0.02	$0.8 \cdot 10^6$	1.9
	0.01	$6.7 \cdot 10^6$	19.1
240	0.02	$0.8 \cdot 10^6$	2.3
	0.01	$6.7 \cdot 10^6$	33.5
1100	0.02	$0.8 \cdot 10^6$	2.2
	0.01	$6.7 \cdot 10^6$	33.5

Fig. 2 compares the experimental and numerical time series of heave displacement and velocity of the device for the three values of b_{PTO}. Qualitatively, the agreement for the three cases is satisfactory in terms of both amplitude and phase. Fig. 2 shows that when b_{PTO}=0 Ns/m, the heave displacement amplitude is maximum, and its value is comparable to the incident wave height (H=0.16 m) since the buoy is freely floating on the surface. As it is expected, the higher the damping coefficient of the PTO system, the lower the amplitude of the heave displacement and velocity, reaching a reduction of over 2/3 when comparing b_{PTO}=0 Ns/m with b_{PTO}=1100 Ns/m. Fig. 2 also proves that, regardless of the value of b_{PTO}, the period of the heave movement is always equal to the wave period (T=1.5 s) and the phase lag between heave displacement and velocity is of π/2 rad. On the other hand, looking closely at Fig. 2 it can be noted that varying b_{PTO} causes a slight phase shift in the time series of both Z and v_z. This shift was analysed in detail by Zang et al. (2018).

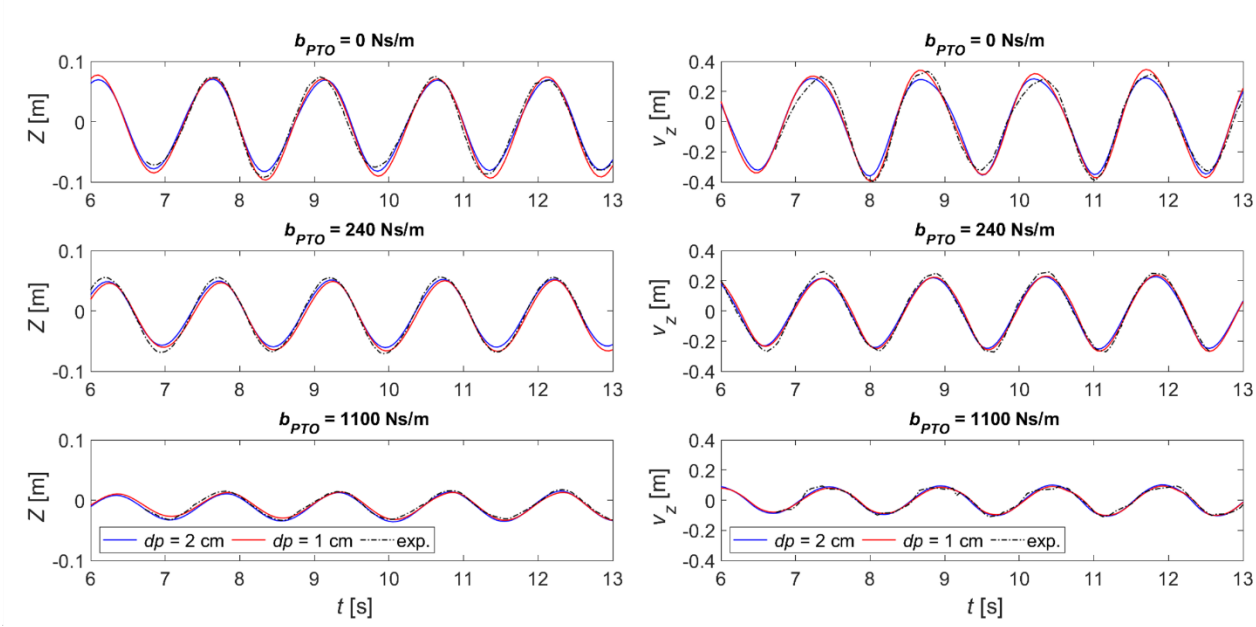

Fig. 2. Numerical and experimental time series of heave displacement (a), and velocity (b) of the point-absorber for b_{PTO} = 0, 240 and 1100 Ns/m.

To quantify the accuracy of the results, the index of agreement d_1 defined by Willmott et al. (1985) is used here as non-dimensional error estimator:

$$d_1 = 1 - \frac{\sum_{n=1}^{N}|C_n - E_n|}{\sum_{n=1}^{N}(|C_n - \bar{E}| + |E_n - \bar{E}|)} \tag{13}$$

where N is the total number of records of the studied variable, C and E are, respectively, the values obtained numerically and experimentally (or theoretically when possible) and the overbar represents the average. The index of agreement is bounded between 0 and 1, where 1 means that the numerical and experimental (or theoretical) time series are coincident.

Table 2 collects the different values of d_1 for the time series of Z and v_z shown in Fig. 2, i.e. for three values of b_{PTO} and two values of dp. The index of agreement ranges from 0.91 to 0.94 in all cases, which implies a very high level of coincidence between the numerical and experimental time series. Table 2 also shows that the improvement in accuracy obtained when using the finest resolution (dp=0.01 m) is barely noticeable. Consequently, the lower resolution (dp=0.02 m) was chosen for all simulations hereinafter since the computational time increases tenfold when using dp=0.01 m (see Table 1). This proves the capability of DualSPHysics to reproduce with accuracy the response of a point-absorber under these regular waves for different configurations of the PTO system at very reasonable computational times.

Table 2. Index of agreement of the heave displacement and velocity for each simulation.

b_{PTO} [Ns/m]	dp [m]	d_1	
		Z	v_z
0	0.02	0.93	0.92
	0.01	0.94	0.93
240	0.02	0.94	0.91
	0.01	0.93	0.91
1100	0.02	0.91	0.91
	0.01	0.91	0.91

Five different instants of the simulations with b_{PTO}=0 Ns/m and b_{PTO}=1100 Ns/m (dp=0.02 m) are shown in Fig. 3. Note that the instants cover one complete wave period (in fact, the first and last instants are coincident). The colourmap represents the velocity of the fluid particles in the longitudinal axis. Minimum values are observed at wave troughs and maximum values at the crests. The black solid line represents the initial still water level; it emphasises the differences in the motion of the buoy when varying the damping coefficient of the PTO system. For the frames at 1/4T and 3/4T, it can be easily observed that the heave amplitude is significantly lower using b_{PTO}=1100 Ns/m than using b_{PTO}=0 Ns/m.

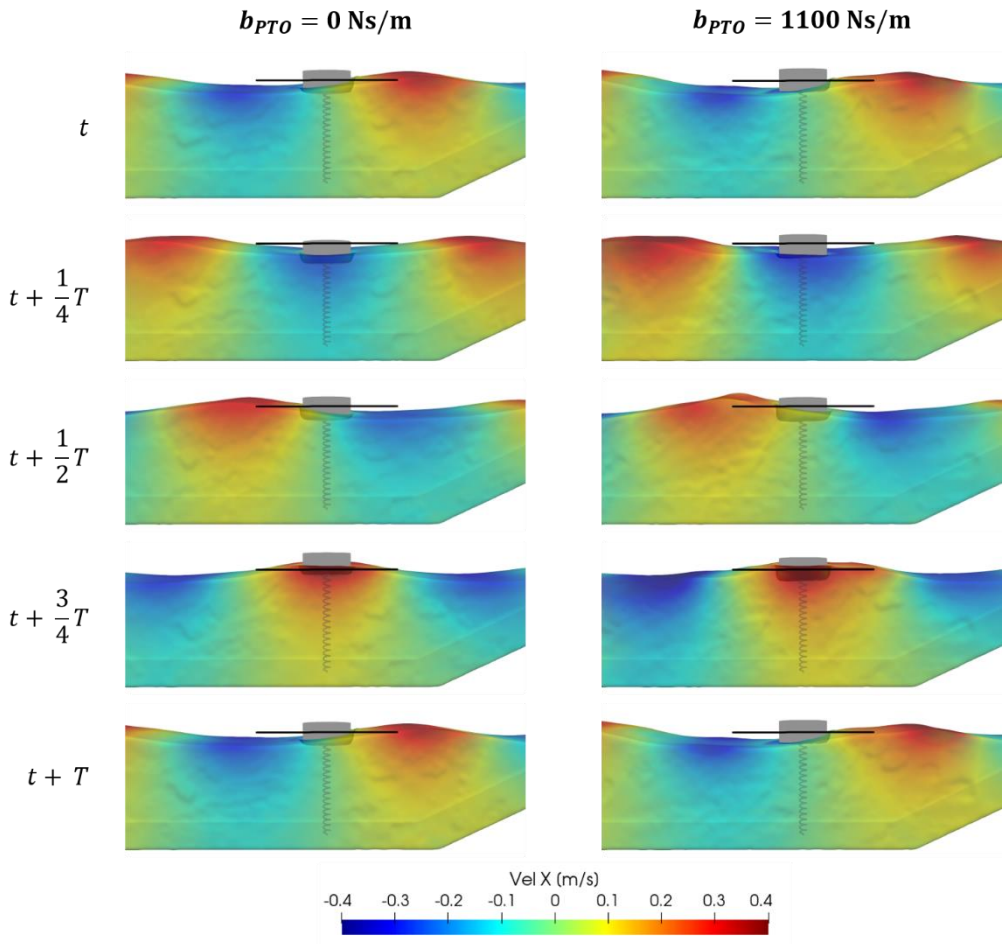

Fig. 3. Different instants of the simulation using DualSPHysics with b_{PTO}=0 and 1100 Ns/m.

4. Efficiency

The previous section has proved the ability of the DualSPHysics numerical code to provide an accurate response of the point-absorber under regular waves of T=1.50 s, H=0.16 m, and d=1.10 m, and for three different values of the damping coefficient. In this section, a study of the evolution of the absorbed power and the system efficiency with the wave frequency, considering the effect of different configurations of the PTO, is performed. Regular waves with the same wave height and depth, but with periods ranging from 0.97 s to 4.40 s are simulated for several values of the PTO damping coefficient.

First, it is important to define the wave power per meter of width of the wave front, denoted as J and obtained as indicated in Falnes (2002):

$$J = \frac{1}{16}\rho g H^2 \frac{\omega}{k}\left[1 + \frac{2kd}{\sinh(2kd)}\right] \tag{14}$$

where k=2π/L is the wavenumber and ω=2π/T the angular wave frequency.

The absorbed power by the point-absorber under study is analysed by comparison with J in order to obtain the efficiency for different regular wave conditions. Table 3 contains the characteristics of the regular waves that are simulated, namely period (T), angular frequency (ω), wavelength (L), Ursell number (Ur) and wave power per meter of width of the wave front (J).

Table 3. Wave conditions simulated in the efficiency analysis.

T [s]	ω [rad/s]	L [m]	Ur	J [W/m]
0.97	6.48	1.47	0.26	23.8
1.00	6.28	1.56	0.29	24.56
1.05	5.98	1.72	0.36	25.84
1.09	5.76	1.85	0.41	26.92
1.15	5.46	2.06	0.51	28.58
1.20	5.24	2.24	0.60	30.04
1.30	4.83	2.61	0.82	33.22
1.50	4.19	3.40	1.39	40.46
1.70	3.70	4.19	2.11	48.14
1.90	3.31	4.98	2.98	55.36
2.10	2.99	5.75	3.97	61.74
2.40	2.62	6.87	5.68	69.56
2.80	2.24	8.33	8.34	77.28
3.30	1.90	10.10	12.27	83.84
4.40	1.43	14.15	23.23	91.86

In Fig. 4, the Le Méhauté abacus (Le Méhauté, 1976) shows the most appropriate theory to model each regular wave. All of them fall within the Stokes' theory zone of the abacus: waves with period equal and lower than 1.70 s are of third order, being the rest second order Stokes' waves. Nevertheless, all of them are generated according to the second order theory implemented in DualSPHysics (Madsen, 1971). This implies the assumption that the third order terms of the Stokes' perturbative series are negligible with respect to the second order terms. Furthermore, to guarantee that the second order terms do not cause spurious crests and troughs that may prevent the wave free-surface profile from having a constant form in time, it is required that the second order terms are significantly lower than the first order terms of the Stokes' expansion. The Ursell number (Ursell, 1953), mathematically defined as $Ur=HL^2/d^3$, provides the relation between the amplitudes of the second and first order terms of the free-surface elevation. According to the theory developed by Madsen (1971) and implemented in DualSPHysics, the wave free-surface profile is constant if $Ur<8\pi^2/3$. Table 3 shows that the Ursell number increases with the wave period but it is always below the required threshold.

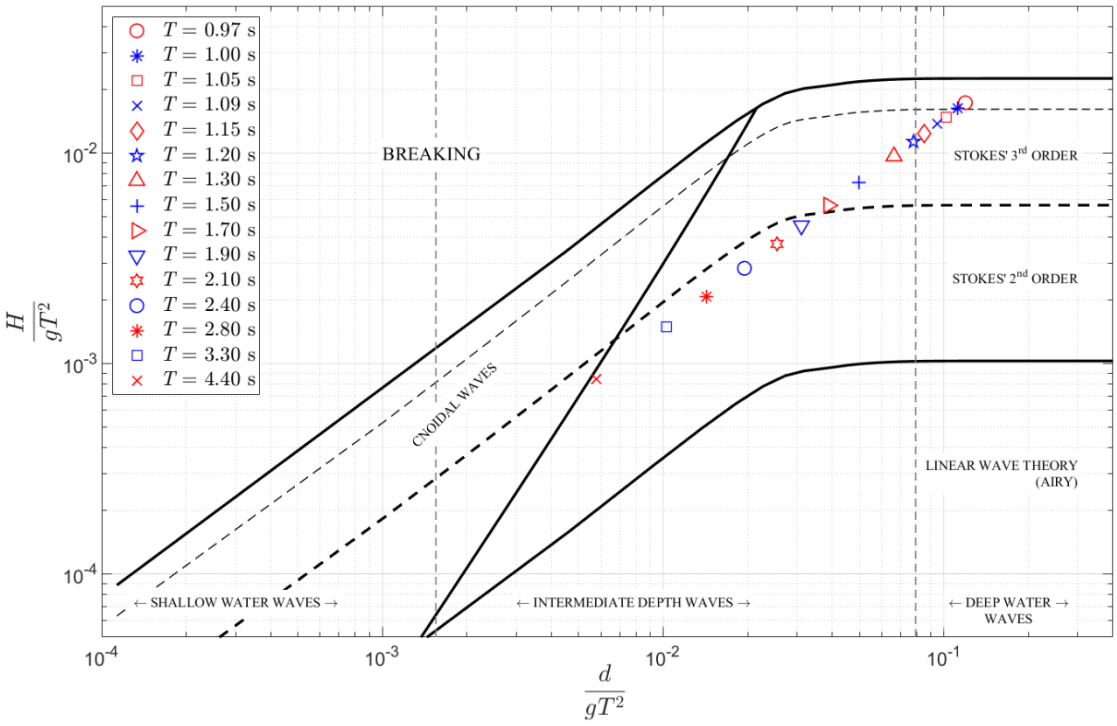

Fig. 4. Regular wave conditions as classified in Le Méhauté abacus.

The numerical tank used to perform the efficiency analysis is the same as used before (Fig. 1). The width and still water depth are the same used for the validation case. However, since the buoy is located one wavelength away from the piston and one quarter of wavelength away from the beginning of the beach, the total length of the domain now varies in accordance with the wavelength of each condition. The slope of the dissipative beach, α, is chosen for each wave condition such that, in combination with the numerical damping previously explained, it yields a reflection coefficient always lower than 6%. Specifically, α=1:2 is used for regular waves with T=1.5 s and lower; α=1:4 for T=1.7, 1.9, 2.1 and 2.4 s; α=1:4 for T=2.8 and 3.3 s; and α=1:12 for T=4.4 s.

The power absorbed by the device and its energetic efficiency are computed as explained below. The instant wave power captured by the WEC is proportional to the damping force of the PTO system, given by Eq. (9), following:

$$P_{abs}(t) = F_{PTO}(t) \cdot v_z(t) = b_{PTO} \cdot v_z^2(t) \tag{15}$$

The integral of Eq. (15) over a time period provides the averaged power absorbed by the device:

$$P_a = \frac{1}{T}\int_{t_0}^{t_0+T} P_{abs}(t)dt \tag{16}$$

Taking a constant time interval Δt, the averaged absorbed power can be further approximated by a discrete summation:

$$P_a = \frac{1}{N}\sum_{n=1}^{N} P_{abs}(t_0 + n\Delta t) \tag{17}$$

where T=N·Δt, being N the total number of records taken in a period.

Budal and Falnes (1975), Evans (1976), and Newman (1976) independently derived the expression for the theoretical maximum absorbed power by an axisymmetric body oscillating only in heave, such as the point-absorber considered in this paper, as:

$$P_{a,max} = \frac{J}{k} \tag{18}$$

where J denotes the wave power per meter of width of the wave front (Eq. 14) and k is the wavenumber.

The efficiency of the wave energy converter can be characterised as the ratio between the power absorbed by the device and its theoretical maximum:

$$\frac{P_a}{P_{a,max}} = 2\pi \frac{P_a}{JL} \tag{19}$$

The capture width (CW) and capture width ratio (CWR) are two parameters often used when performing an efficiency analysis. The former represents the width of the wave front that is being completely absorbed by the device, whereas the latter represents the ratio between the absorbed power and the available power contained in the wave interacting with the device, which is defined as $P_w=JD$ (being D the buoy diameter). They can be mathematically described as:

$$CW = \frac{P_a}{J} \tag{20}$$

$$CWR = \frac{P_a}{P_w} \tag{21}$$

Capture width has units of meters, hence CWR is a dimensionless parameter given by CW over the device dimension perpendicular to wave propagation, in this case the buoy diameter D. Their maximum values can be obtained from Eq. (18). Therefore, the energetic efficiency can also be characterised using the ratio CW/CW_{max} or CWR/CWR_{max} since:

$$\frac{CWR}{CWR_{max}} = \frac{CW}{CW_{max}} = \frac{P_a}{P_{a,max}} = 2\pi \frac{P_a}{JL} \tag{22}$$

The response of the heaving point-absorber is highly frequency-dependent, being the energy conversion more important near the resonance condition. When the WEC is operating at resonance, its heaving velocity and the excitation force are in phase. The excitation force is made up of the force due to the non-perturbed incoming wave acting on the WEC (Froude-Krylov force) and the force due to the diffraction of the flow bypassing the buoy. As shown in Falnes (2002), the resonance condition is automatically satisfied when the wave frequency matches the natural frequency of the device, which is given by:

$$\omega_0 = \sqrt{\frac{\rho g A_{wet}}{M + m_{add}(\omega)}} \tag{23}$$

where A_{wet} is the wetted surface (cross-section of the cylinder), M is the mass of the buoy, and m_{add} is the added mass. The added mass term is due to the radiated waves emitted by the oscillating buoy, and it varies with the wave frequency, which implies that the natural frequency is frequency-dependent as well. The open-source solver NEMOH (Babarit and Delhommeau, 2015) is used to obtain the added mass. NEMOH is a boundary element method (BEM) code that solves the radiation-diffraction problem assuming linear waves and neglecting viscosity. Note that the calculation of the natural frequency is only used here to define the non-dimensional variable ω/ω_0, which allows identifying whether the point-absorber is operating near its resonance condition. Therefore, the simplifications made to obtain the natural frequency have no effect on the calculus of the absorbed power, since this is obtained from the heave velocity time series computed with DualSPHysics, which simulates with accuracy non-linear waves and does include viscous forces.

Fig. 5 shows the evolution of the absorbed power and the energetic efficiency as functions of the ratio ω/ω_0 for different values of b_{PTO}, namely 240, 480, 720, and 1100 Ns/m. When ω tends to zero or infinity, so does the ratio ω/ω_0, since ω_0 takes finite (and non-zero) values for all ω, and the absorbed power and energetic efficiency tend to be zero. Both the absorbed power and the energetic efficiency reach a maximum between $\omega/\omega_0=0$ and $\omega/\omega_0=1$, respectively. However, the wave frequency that maximises P_a is different from the one that maximises the energetic efficiency. This is due to the fact that the wave power per meter of width of the wave front, Eq.

(14), decreases when the wave frequency increases, as shown in Table 3. Fig. 5(a) shows that the maximum absorbed power occurs at around ω/ω_0=0.5 for b_{PTO}=1100 Ns/m, and around ω/ω_0=0.8 for b_{PTO}=240 Ns/m. The peak of P_a tends to appear at frequencies close to the natural frequency as the damping coefficient of the PTO decreases. A similar behaviour is observed in Fig. 5(b) for the energetic efficiency (defined here as CWR/CWR_{max}) but, in this case, the peak of efficiency takes place at frequencies slightly lower than ω_0 for all the values of b_{PTO}. Note as well that the maximum energetic efficiency is higher as b_{PTO} decreases, being around 0.6 for b_{PTO}=1100 Ns/m and close to 0.9 for b_{PTO}=240 Ns/m.

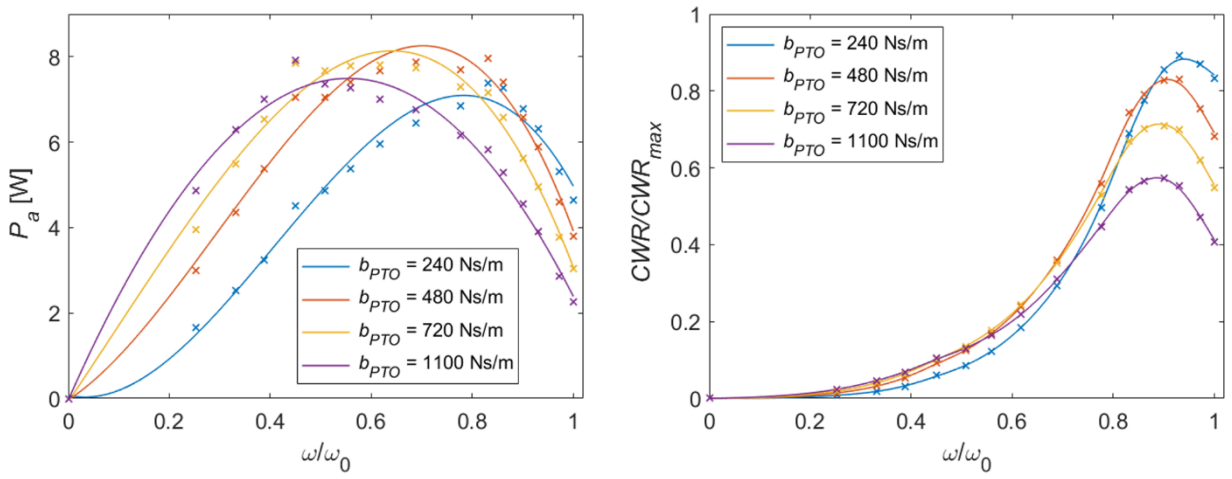

Fig. 5. Variations of absorbed power (a) and CWR/CWR_{max} (b) with the frequency of regular waves for different values of b_{PTO}.

Fig. 6 shows the dependence on the damping coefficient of the PTO of the absorbed power (P_a) and energetic efficiency (CWR/CWR_{max}) for three different wave frequencies, namely ω/ω_0=0.51, 0.77 and 1.00. When b_{PTO}=0 Ns/m, the PTO system is disconnected and the wave energy is not being harvested, as indicated mathematically in Eq. (15). On the other hand, when b_{PTO} tends to infinity the device response is overdamped and the absorbed power, thus the efficiency, tends asymptotically to zero. There is a value of b_{PTO} for each wave condition that maximises both P_a and CWR/CWR_{max}. When the device is operating at resonance (ω/ω_0=1), the maximum efficiency is achieved when b_{PTO} is between 60 and 240 Ns/m. Comparing the three different wave conditions shown in Fig. 6, it is clear that the further away from resonance, the higher the optimum value of b_{PTO} and the less steep the curves, i.e. the range of b_{PTO} for which P_a and energetic efficiency are near their maximum is wider.

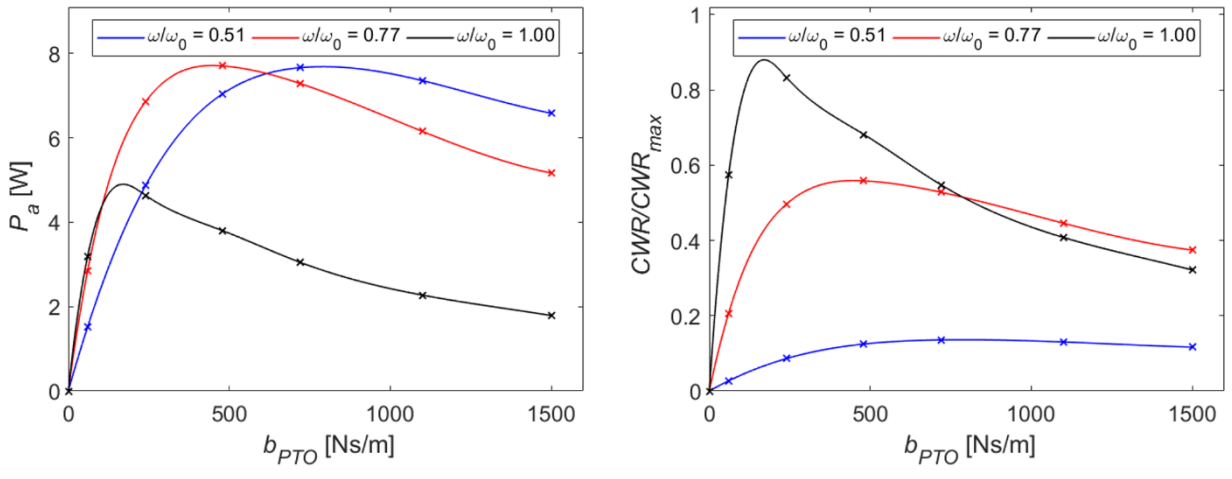

Fig. 6. Variations of absorbed power (a) and CWR/CWR_{max} (b) with b_{PTO} for different values of ω/ω_0.

5. Survivability

The final numerical analysis with the point-absorber under study in this work is related to survivability. As previously introduced, the use of an SPH-based code presents several advantages, which make the simulation of violent impacts between sea waves and floating devices easy and straightforward. In this section, the loads acting on the device under an extreme wave condition are obtained numerically with DualSPHysics. Different survival strategies are defined, considering the effects of submerging the device and simulating the WEC fixed or oscillating. A simplified structure is assumed to show a general methodology that may be followed to design the structure for a point-absorber.

5.1. Extreme wave description

Puertos del Estado (www.puertos.es) provides measures of the sea-state under extreme weather conditions in the northern coast of Spain. The survivability of the WEC is analysed at a location in the north coast of Spain 4 km offshore from the Port of Gijón, where the water depth is 54 m. A directional buoy owned by Puertos del Estado provides the irregular extreme sea-state at this location from data recorded from March 2004 to January 2017. A storm is defined as a situation during which the significant wave height H_s (mean wave height of the highest third of the records) exceeds a predefined threshold, following the Peak Over Threshold method. The irregular sea-state of each storm is characterised by the maximum H_s in a five-day period and its associated peak period, T_p, is obtained from an empirical equation based on a least-squares fitting. Given a desired lifetime of the device L_{WEC}, and a limit state which has an associated exceedance probability P_L, the design wave height H_d of the irregular extreme sea-state at the specified location can be obtained as explained below. The exceedance probability P_L is the probability that the design wave height H_d is exceeded during the lifetime L_{WEC} and is given by:

$$P_L(H_d) = 1 - \left(1 - P_{ann}(H_d)\right)^{L_{WEC}} \tag{24}$$

where $P_{ann}(H_d)$ is the probability that H_d is exceeded in a year, defined as

$$P_{ann}(H_d) = 1 - exp\left(-\lambda\left(1 - F_w(H_d)\right)\right) \tag{25}$$

being λ the average number of storms in a year and F_w the Weibull distribution (Weibull, 1951) of exceedance of wave height, given by

$$F_w(H_d) = 1 - exp\left(-\left(\frac{H_d - \alpha_w}{\beta_w}\right)^{\gamma_w}\right) \tag{26}$$

The parameters α_w, β_w and γ_w define the specific Weibull distribution and are provided by Puertos del Estado, along with λ. Considering a lifetime L_{WEC} of 22 years and an exceedance probability P_L=0.53, corresponding to the Damage Limitation limit state, a design wave height of H_d=0.985 m (after 1:10 Froude scaling) is obtained from Eqs. (24) – (26). The corresponding peak period, T_p, is calculated from the design wave height by means of the empirical equation provided by Puertos del Estado, obtaining a value of T_p=5.30 s, calculated at 1:10 model scale.

These design wave height and peak period define the irregular extreme sea-state at a specific location for the Damage Limitation limit state of a device with a lifetime of 22 years. A complete statistic representation of a real sea state consists of an irregular wave train of at least 300 waves (Boccotti, 2004). The importance of the time series duration in wave-structures interactions has been highlighted by other authors (e.g. Romano et al., 2015). In practice, 1000 waves are employed to represent real sea states, when reproduced experimentally. Numerical models based on full Navier-Stokes equations, either mesh-based or meshless, must often cope with huge computational costs associated with such long test durations, especially for 3-D modelling. Therefore,

instead of a full sea state, a focused wave group is simulated. To account for the possibility of a sporadic freak wave of wave height significantly higher than H_d within this sea-state, a focused wave is defined as follows: a 1000-wave train is used to build the Rayleigh distribution of the wave height and the one with only 3% probability to be exceeded is selected as the focused wave height, being in this case H_f=1.31 m.

In the present work, a unidirectional crest-focused wave, defined according to the so-called NewWave method (Whittaker, 2017) is employed. The NewWave linear theory developed by Tromans et al. (1991) defines the free-surface elevation $\eta(x,t)$, which is related to the Fourier Transform of the sea state power density spectrum $S(\omega)$, as a linear superposition of N wave modes

$$\eta(x,t) = \frac{A_{cr}}{\sigma^2} \sum_{n=1}^{N} S(\omega_n) \cos\left(k_n(x - x_f) - \omega_n(t - t_f)\right) \Delta\omega \tag{27}$$

being $\sigma^2=\Sigma S(\omega_n)\Delta\omega$ the variance of the discrete irregular sea state, ω_n and k_n the angular frequency and wavenumber of each n-mode, and x_f and t_f the position and time, respectively, at which the free-surface elevation reaches its maximum, $\eta(x_f, t_f)=A_{cr}$, i.e. where and when the wave train *focuses*. Whittaker (2017) noted that whenever a focused wave group is generated by a wavemaker that moves according to the NewWave linear theory spurious waves arise. To prevent this, the second-order wave generation theory proposed by Madsen (1971) is used here. Correction for bound-long waves is neglected in the present application.

The generation and propagation of the focused wave at a desired focus location is validated by running a 2-D simulation without the WEC. The focused wave is generated using H_f=1.31 m, T_p=5.30 s and d=5.40 m (obtained after the 1:10 Froude scaling of the sea depth). The free-surface elevation measured numerically with DualSPHysics at x_f=15.00 m is compared with the second-order analytical solution given by Madsen (1971) in Fig. 7. The crest-focused wave reaches the focus location, where the mid-point of the device will be placed, at t_f=18.30 s. The matching between the numerical and theoretical free-surface elevation is quantified by means of the index of agreement defined in Section 3. By applying Eq. (13) to the time series of η shown in Fig. 7, a value of d_I=0.86 is obtained, which validates the generation and propagation of the focused wave with DualSPHysics.

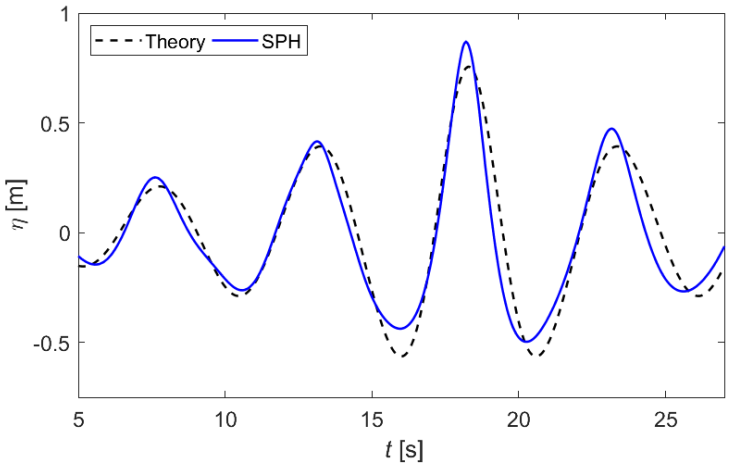

Fig. 7. Numerical and theoretical time series of the free-surface elevation at x_f.

5.2. Numerical tank and setup of the cases

Fig. 8 depicts a lateral view of the 3-D numerical tank employed for the simulations hereinafter. As in the previous cases, the tank width is twice the diameter of the buoy, and periodic boundary conditions are applied to the lateral walls. Nevertheless, the still water level is now at d=5.40 m above the sea bottom, and the mid-point of the device is placed 15.00 m away from the wavemaker. In addition, a different anti-reflective beach has to be arranged at the end of the tank because of the high energetic content of the wave to be absorbed. To guarantee an adequate wave dissipation, a 1:3 steep beach beginning at 5.00 m from the axis of the buoy acts together with a numerical damping, as defined in Eqs. (10) and (11). The wavemaker is a piston-type one that

moves according to a steering function, which guarantees that the focused wave described in the previous section focuses at x_f (Fig. 7).

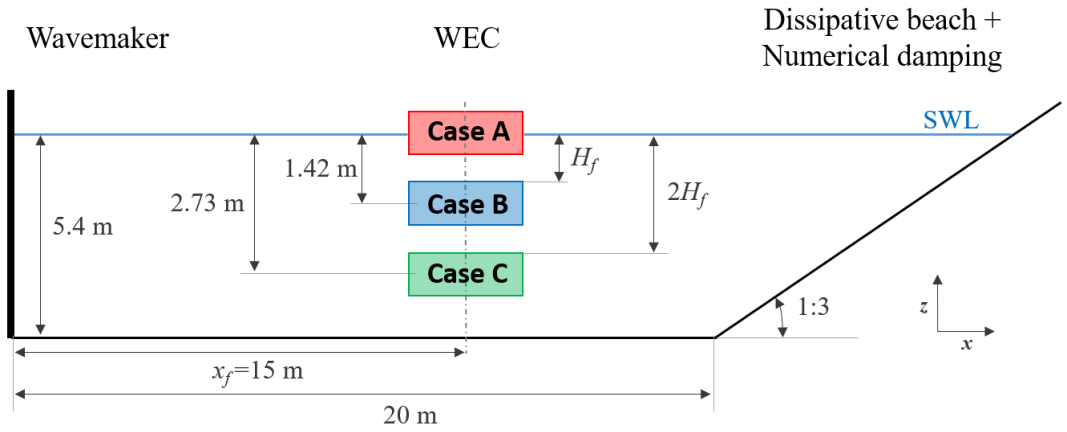

Fig. 8. Numerical tank configuration for the different cases in the survivability study.

Fig. 8 also illustrates the different depths to submerge the device, being H_f=1.31 m as explained in the previous section. Six different cases are considered in the survivability study. In all of them the PTO system is temporarily switched off to avoid an eventual damage to the most expensive and fragile part of the WEC, which means b_{PTO}=0 Ns/m. The loads exerted on the device are measured for the different scenarios that differ about the degrees of freedom of motion and the location of the device. Table 4 helps to define the different scenarios, where they are named with an upper-case letter and a number. The letter refers to the different levels of submergence, denoting A, B, and C that the centre of mass of the device is at still water level (SWL), submerged 1.42 m below SWL, or submerged 2.73 m below SWL, respectively. The number that follows refers to the degrees of freedom of the device, being 1 only-heave motion and 2 all degrees of freedom restricted, i.e. the device is completely fixed.

Table 4. Setup of the different cases.

Case	Initial depth [m]	Fixed / Heaving
A1	0 (SWL)	Heaving
A2	0 (SWL)	Fixed
B1	1.42	Heaving
B2	1.42	Fixed
C1	2.73	Heaving
C2	2.73	Fixed

When the buoy is fully submerged, the difference between the upward buoyancy force (equal to the weight of the displaced fluid) and the downward force due to its own weight results in a vertical net force F_{net}. Since the density of the buoy is half the density of the fluid, the net force is positive (upward) and equal to the weight of the buoy: F_{net}=212 N. In the cases B1 and C1, the device is fully submerged and heaving around the desired depth, thus it is necessary to have a downward force that balances the upward net force in still water. Numerically, it can be modelled as an elastic force (F_s) using:

$$F_s(t) = -k_s\big(l(t) - l_{eq}\big) \tag{28}$$

such that F_s (t=0)=-F_{net} and that the spring length $l(t)$ is longer than the equilibrium length, l_{eq}, during the simulation to guarantee that the spring force direction remains unchanged. Setting the spring stiffness to k_s=321 N/m, these requirements are satisfied, and the buoy is able to oscillate at the desired depth.

5.3. Results

The focused wave presented in Section 5.1 is simulated for each scenario described in Table 4 using the numerical tank shown in Fig. 8. The forces acting on the device in each case are calculated using the post-processing tools of DualSPHysics. Figs. 9 and 10 show the time series of the forces in the x (longitudinal direction) and z (vertical direction) axis, respectively, along with the theoretical time series of the free-surface elevation at x_f in the secondary axis. For the sake of clarity, the results are split into two plots in both figures, corresponding to the cases where heave motion is allowed (a) and where the device remains fixed (b). Note that, since the focused wave is unidirectional (along the x-axis) and the geometry of the buoy is axially symmetric, the force acting in the y-axis is not taken into account.

As shown in Fig. 9, the time series of the force in the x-direction, F_x, follows the trend of the free-surface elevation, η. The maximum values of the horizontal force take place approximately during the peaks of the elevation time series. Fully submerging the buoy significantly reduces the maximum amplitude of F_x, since it is lower for cases B and C than for cases A. This difference in the behaviour of F_x with the submergence is due to the variation of the longitudinal acceleration of the fluid in the vertical direction. Comparing the results of F_x for the heaving and fixed devices initially placed at the same depth, the magnitude of F_x is lower when the device is fixed. However, the effect of holding the device fixed is minimized significantly when the WEC is completely submerged.

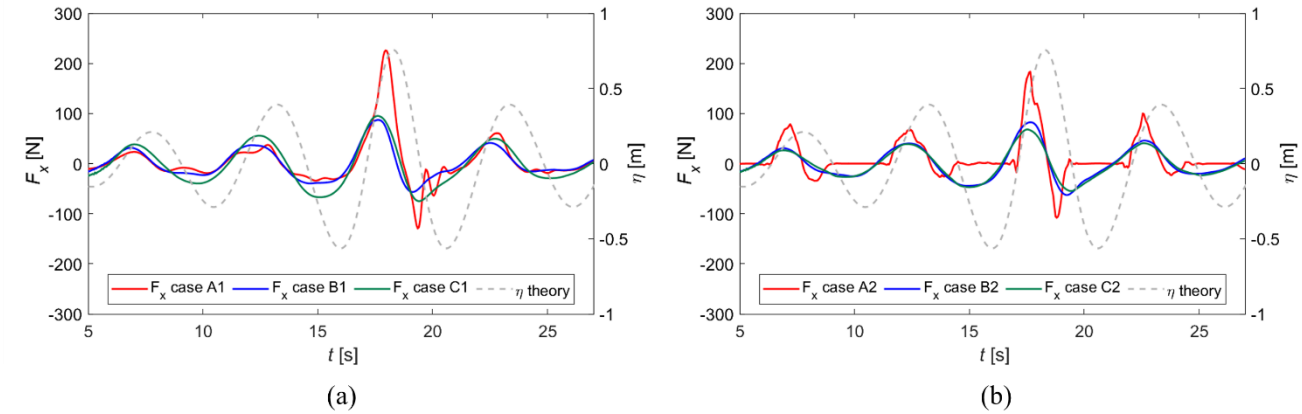

Fig. 9. Time series of the forces in the x-direction (F_x) acting on the heaving (a) and fixed (b) device for each case.

Fig. 10 shows that the forces in the z-direction, F_z, oscillate around zero when the device is initially at SWL and around the value of the vertical net force (F_{net}=212 N) when it is fully submerged, since the density of the floater is lower than the density of the water. Although a slightly lower amplitude of F_z is observed for case C1, the values of the vertical force are very similar for the cases when the device is completely submerged (cases B1, B2, C1, C2), regardless of whether it remains fixed or it oscillates. However, comparing the results of F_z for the heaving and fixed device initially semi-submerged (cases A1 and A2, respectively), a great difference can be observed in Fig. 10. As a matter of fact, configuration A1 minimises the vertical force, while configuration A2 maximises it.

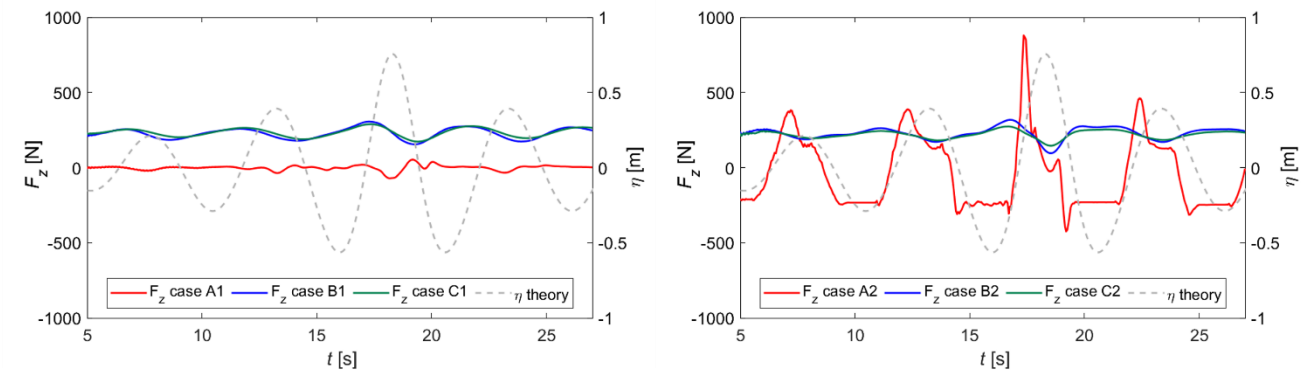

Fig. 10. Time series of the forces in the z-direction (F_z) acting on the heaving (a) and fixed (b) device for each case.

In absence of any stronger physical phenomenon, the behaviour of F_z is driven by the vertical acceleration of the fluid particles during wave propagation. This acceleration is in antiphase with the wave free-surface elevation, so that F_z will be in antiphase with η as well. Different situations can be found in Fig. 10. Case A1 (where the WEC is moving at SWL) and cases B2 and C2 (where the WEC is fixed at a certain depth) follow the general behaviour mentioned before, i.e., F_z is in antiphase with η. However, in cases B1 and C1 (where the WEC is submerged and heaving), the spring force, needed to keep the device oscillating at the given depth, slightly shifts F_z, being consequently in phase with the heave motion.

The atypical behaviour of the forces observed for case A2 (fixed device at SWL) deserves a more detailed explanation. Fig. 7 showed that the absolute maximum and minimum values of the free-surface elevation are clearly higher than the height of the buoy. Therefore, when the device is fixed at SWL, the focused wave crest leads to a huge and sudden overtopping, whereas the troughs cause the free surface to be below the bottom of the cylinder. In this way, the forces acting on the WEC increase suddenly during the crest of the focused wave. On the other hand, the only force acting on the device during the troughs is its own weight, which explains the interval of time observed in Figs. 9 and 10 during which F_x and F_z are constant, specifically at F_x=0 N and F_z=212 N. It is also worth noting that there is an instant, after the wave crest has passed the buoy and before the next trough arrives, in which the device is also bearing the weight of the overtopping water that remains on its top surface, leading to the negative peaks of F_z.

The analysis of the forces alone does not clearly determine the best and worst-case scenario. If only forces in the x-axis are considered, case A1 would seem to be the most harmful to the structure. However, case A1 would be the least harmful when only vertical forces are considered. Thus, a criterion that takes into account both contributions is needed.

The structure considered in the present paper is a simplification of the one depicted in Zang et al. (2018), which assumes that the buoy is connected to the seabed by means of a clamped rod of circular cross-section. In this manner, it is possible to characterise the effects of the wave field on the buoy and its structure by performing an elastic verification based on the yield criterion. The Designers' Guide to EN 1993-1-1 Eurocode 3 defines the yield criterion for a critical point of a steel cross-section in the following general way:

$$\left(\frac{\sigma_x}{f_y/\gamma_{M0}}\right)^2+\left(\frac{\sigma_z}{f_y/\gamma_{M0}}\right)^2-\left(\frac{\sigma_x}{f_y/\gamma_{M0}}\right)\cdot\left(\frac{\sigma_z}{f_y/\gamma_{M0}}\right)+3\cdot\left(\frac{\tau}{f_y/\gamma_{M0}}\right)^2\leq 1 \tag{29}$$

where σ_x is the longitudinal local stress, σ_z is the transverse local stress, τ is the local shear stress, f_y is the yield stress of the material and γ_{M0} is the partial factor, which is taken as 1. Since the structure considered here is a slender rod of circular cross-section, the transverse and shear stresses are negligible compared with the longitudinal stress. Thus, the yield criterion in the present application is simply given by:

$$\left(\frac{\sigma_x}{f_y}\right)^2 \leq 1 \tag{30}$$

where the longitudinal local stress is defined as:

$$\sigma_x = \frac{F_z}{A_{rod}} + \frac{F_x l_{arm}}{W_{rod}} \tag{31}$$

being $A_{rod}=\pi D_{rod}^2/4$ the cross-section area, $W_{rod}=\pi D_{rod}^3/32$ the elastic section modulus, D_{rod} the diameter of the rod and l_{arm} the lever arm (distance between the point of application of the forces in the floater and the base of the rod). A value of the yield criterion (Eq. 30) higher than 1 indicates a failure of the structure under the load produced by the event considered in the survivability analysis. Eq. (31) shows that the elastic verification considers the contribution of both F_x and F_z. Nevertheless, since $l_{arm} \gg D_{rod}$ and therefore $W_{rod}/l_{arm} \ll A_{rod}$, its behaviour is dominated by the term containing F_x.

The time series of the yield criterion for each scenario are obtained assuming a rod made of S235 steel (f_y=235 MPa) and for different values of D_{rod}. The maximum value for each case is presented in Table 5. If the diameter of the rod is 40 mm and the buoy is heaving at SWL (case A1), the maximum value of the yield criterion is very close to 1 and therefore, the structure of the WEC could collapse under the extreme event considered here. To avoid this, three strategies are studied: i) fixing the buoy, ii) submerging the buoy, and iii) increasing the rod diameter of the structure. Table 5 shows that when the device is initially placed at SWL, restraining all its movements reduces by approximately one third the value of the yield criterion. Submerging the buoy 1.42 m below SWL (cases B1 and B2) reduces over thirteen times the maximum yield criterion, which proves that the common practice of submerging the device is highly effective. If the initial depth of submergence is increased from 1.42 to 2.73 m below SWL (cases C1 and C2), the maximum yield criterion is approximately halved, which is, in fact, a very slight reduction compared with the one obtained between cases A and B. The elastic verification can also be satisfied by increasing the diameter of the rod. However, an increase of 50% in the rod diameter (from D_{rod}=40 mm to D_{rod}=60 mm) is needed in order to achieve values of the yield criterion similar to those obtained when fully submerging the buoy.

Table 5. Maximum values of yield criterion for each case.

D_{rod}	Case A1	Case A2	Case B1	Case B2	Case C1	Case C2
40 mm	0.989	0.666	0.068	0.051	0.037	0.016
50 mm	0.259	0.175	0.018	0.013	0.010	0.004
60 mm	0.087	0.059	0.006	0.004	0.003	0.001

The most effective strategy to reduce the wave-induced effects caused by an extreme event on the system is to submerge the device such that the top surface of the buoy is initially H_f below SWL (cases B1 and B2). Increasing the initial depth of immersion (cases C1 and C2) would require an extra economic cost very difficult to justify, since the associated reduction of the yield criterion is minimum. Fixing the device (case B2) reduces slightly the maximum yield criterion with respect to the heaving device (case B1), thus the costs and reliability of the mechanical systems needed in each case should be considered when making that choice.

6. Conclusions

The hydrodynamic response of a point-absorber under regular waves can be accurately obtained with DualSPHysics. The numerical results for different configurations of the PTO system match satisfactorily the experimental results for a given regular wave condition. Once validated, it has been shown that DualSPHysics provides a unique framework to study numerically two key aspects in the design of a WEC: efficiency and survivability under eventual extreme wave conditions.

The power captured by the point-absorber as well as its energetic efficiency have been obtained from the time series of the device motion for a wide range of regular waves, and for several values of the damping coefficient b_{PTO}. It has been shown that when the WEC operates near its resonance condition, the efficiency is maximised. However, the wave frequency at which the absorbed power reaches its maximum depends on the value of b_{PTO}: it approaches the natural frequency (resonance condition) as b_{PTO} decreases. The analysis has also proven that there is a certain configuration of the PTO system that maximises both the absorbed power and the efficiency for each wave condition. In particular, the optimum b_{PTO} value is here between 60 and 240 Ns/m when the point-absorber is operating close to resonance and, it can be also observed that, the further away from this condition the higher the optimum value of b_{PTO}.

The survivability analysis has been conducted by means of a focused wave, whose characteristics are defined from the design spectrum corresponding to a certain limit state and lifetime of a device, placed at a specific location. DualSPHysics has been used to generate and propagate the desired focused wave, and the forces acting on the WEC were numerically computed. The yield criterion quantifies the effect of the loads exerted by the extreme waves on the highly-simplified structure of the WEC for each scenario. It was shown that fully submerging the device when an extreme event occurs is more effective than fixing the device or increasing the size of the structure. Results for the two different depths of submergence show only a slight improvement when submerging the device significantly deeper. This indicates the existence of an optimum depth of submergence. However, its calculation would require a more extensive analysis as well as considering economic factors and its environmental impact.

Acknowledgements

This work was partially financed by the Ministry of Economy and Competitiveness of the Government of Spain under project "WELCOME ENE2016-75074-C2-1-R" and financed by Xunta de Galicia (Spain) under project ED431C 2017/64 ″Programa de Consolidación e Estructuración de Unidades de Investigación Competitivas (Grupos de Referencia Competitiva)" cofunded by European Regional Development Fund (ERDF).

Dr. C. Altomare acknowledges funding from the European Union's Horizon 2020 research and innovation programme under the Marie Sklodowska-Curie grant agreement No.: 792370. Dr J. M. Domínguez acknowledges funding from Spanish government under the program "Juan de la Cierva-incorporación 2017" (IJCI-2017-32592).

Nomenclature

a, b: generic fluid particles
A_{cr}: maximum free-surface elevation of the focused wave (m)
A_{rod}: cross-section area of the rod (m^2)
A_{wet}: wetted surface (m^2)
b_{PTO}: damping coefficient of the PTO system (N·s/m)
c: numerical speed of sound (m/s)
C: numerically obtained value of a generic variable
d: depth (m)
d_1: index of agreement
D: diameter (m)
dp: initial interparticle distance (m)
D_{rod}: rod diameter (m)
E: experimental or theoretically obtained value of a generic variable
$\boldsymbol{f}$: force per unit of mass (m/s^2)
f_y: yield stress of the material (Pa)

F_{net}: vertical net force (N)
F_{PTO}: force exerted by the PTO system (N)
F_s: spring force (N)
F_w: Weibull distribution of exceedance of wave height
F_x: force in the x-direction (N)
F_z: force in the z-direction (N)
$\boldsymbol{g}$: gravitational acceleration (m/s^2)
h: smoothing length (m)
H: wave height (m)
H_d: design wave height (m)
H_f: focused wave height (m)
H_s: significant wave height (m)
I: moment of inertia of the floating object (kg·m^2)
J: wave power per meter of width of the wave front (J/m)
k: wavenumber (rad/m)
k_s: spring stiffness (N/m)
K_R: reflection coefficient
l: spring length (m)
L: wavelength (m)
l_{arm}: lever arm (m)
l_{eq}: equilibrium length (m)
L_{WEC}: lifetime of the WEC (years)
m: mass (kg)
M: mass of the floating object (kg)
m_{add}: added mass (kg)
p: pressure (Pa)
P_a: averaged power captured by the device (J)
$P_{a,max}$: theoretical maximum absorbed power by the device (J)
P_{abs}: instant wave power captured by the device (J)
P_{ann}: annual exceedance probability
P_L: exceedance probability
P_w: available wave power contained within the width of the device (J)
q: generic floating particle
$\boldsymbol{r}$: position (m)
$\boldsymbol{R}$: the centre of mass of the floating object (m)
S: sea state power density spectrum (m^2·s)
t: time (s)
T: wave period (s)
t_f: time when the focused wave reaches its maximum free-surface elevation (m)
T_p: peak period (s)
Ur: Ursell number
$\boldsymbol{v}$: velocity (m/s)
$\boldsymbol{V}$: linear velocity of the floating object (m/s)
$\boldsymbol{v}_{a,0}$: initial velocity of fluid particle a (m/s)
v_z: heave velocity (m/s)
x_0: initial longitudinal position of the numerical damping zone (m)
x_1: final longitudinal position of the numerical damping zone (m)
x_a: longitudinal position of fluid particle a (m)
x_f: position at which the focused wave reaches its maximum free-surface elevation (m)
x, y, z: Cartesian coordinates (m)
W: kernel function

685 W_{rod}: elastic section modulus (m^3)
686 Z: heave displacement (m)
687

688 *Greek letters*

689 α: beach slope
690 β: reduction function coefficient
691 α_w, β_w and γ_w: Weibull distribution parameters
692 γ: polytropic constant
693 γ_{M0}: partial factor of the cross-section
694 η: free-surface elevation (m)
695 λ: average number of storms in a year
696 Π: artificial viscosity ($m^5/kg \cdot s^2$)
697 ρ: density (kg/m^3)
698 ρ_0: reference density (kg/m^3)
699 σ^2: variance of the discrete irregular sea state (m^2)
700 σ_x: longitudinal local stress (Pa)
701 σ_z: transverse local stress (Pa)
702 τ: local shear stress (Pa)
703 $\boldsymbol{\Omega}$**:** rotational velocity of the floating object (s^{-1})
704 ω: the angular wave frequency (rad/s)
705 ω_0: natural frequency (rad/s)
706

707 *Acronyms*

708 BEM: Boundary Element Method
709 CFD: Computational Fluid Dynamics
710 CW: Capture Width
711 CWR: Capture Width Ratio
712 PTO: Take-Off system
713 SPH: Smoothed Particle Hydrodynamics
714 SWL: Still Water Level
715 WCSPH: Weakly Compressible Smoothed Particle Hydrodynamics
716 WEC: Wave Energy Converter
717

718

719 **References**

720 Ahamed, R., McKee, K., Howard, I., 2020. Advancements of wave energy converters based on power take off
721 (PTO) systems: A review. Ocean Engineering 204, 107248.

722 Altomare, C., Domínguez, J.M., Crespo, A.J.C., González-Cao, J., Suzuki T., Gómez-Gesteira, M., Troch, P.,
723 2017. Long-crested wave generation and absorption for SPH-based DualSPHysics model. Coastal
724 Engineering 127, 37-54.

725 Altomare, C., Viccione, G., Tagliafierro, B., Bovolin, V., Domínguez, J.M., Crespo, A.J.C., 2018. Free-Surface
726 Flow Simulations with Smoothed Particle Hydrodynamics Method using High-Performance Computing,
727 in: Ionescu, A. (Ed.), Computational Fluid Dynamics - Basic Instruments and Applications in Science.
728 InTech, Rijeka.

729 Babarit, A., Delhommeau, G., 2015. Theoretical and numerical aspects of the open source BEM solver NEMOH.
730 In: 11th European Wave and Tidal Energy Conference (EWTEC2015).

731 Beatty, S.J., Hall, M., Buckham, B.J., Wild, P., Bocking, B., 2015. Experimental and numerical comparisons of
732 self-reacting point absorber wave energy converters in regular waves. Ocean Engineering 104, 370-386.

733 Boccotti, P., 2004. Idraulica Marittima. UTET Università.

734 Bozzi, S., Besio, G., Passoni, G., 2018. Wave power technologies for the Mediterranean offshore: Scaling and
735 performance analysis. Coastal Engineering 136, 130-146.

736 Brito, M., Canelas, R.B., García-Feal, O., Domínguez, J.M., Crespo, A.J.C., Ferreira, R.M.L., Neves, M.G.,
737 Teixeira, L., 2020. A numerical tool for modelling oscillating wave surge converter with nonlinear
738 mechanical constraints. Renewable Energy 146, 2024-2043.

739 Budal, K., Falnes, J., 1975. A resonant point absorber of ocean-wave power. Nature 256, 478-479.

740 Canelas, R.B., Domínguez J.M., Crespo, A.J.C., Gómez-Gesteira M., Ferreira R.M.L., 2015. A Smooth Particle
741 Hydrodynamics discretization for the modelling of free surface flows and rigid body dynamics.
742 International Journal for Numerical Methods in Fluids 78, 581-593

743 Canelas, R.B., Brito, M., Feal, O.G., Domínguez, J.M., Crespo, A.J.C., 2018. Extending DualSPHysics with a
744 Differential Variational Inequality: modeling fluid-mechanism interaction, Applied Ocean Research 76,
745 88-97.

746 Chongwei, Z., Longtan, S., Wenli, S., Qin, S., Gang, L., Xunqiang, L., Xiaobin, C., 2014. An assessment of
747 global ocean wave energy resources over the last 45 a. Acta Oceanol. Sin 33, 92-101

748 Coe, R., Yu, Y-H., Van Rij, J., 2018. A survey of wec reliability, survival and design practices. Energies 11(1),
749 4.

750 Coe, R.G., Rosenberg, B.J., Quon, E.W., Chartrand, C.C., Yu, Y-H., Van Rij, J., Mundon, T.R., 2019. CFD
751 design load analysis of a two-body wave energy converter. Journal of Ocean Engineering and Marine
752 Energy 5(2), 99–117.

753 Crespo, A.J.C., Domínguez, J.M., Rogers, B.D., Gómez-Gesteira, M., Longshaw, S., Canelas, R., Vacondio, R.,
754 Barreiro, A., García-Feal, O., 2015. DualSPHysics: open-source parallel CFD solver on Smoothed
755 Particle Hydrodynamics (SPH). Computer Physics Communications 187, 204-216.

756 Crespo, A.J.C., Altomare, C., Domínguez, J.M., González-Cao, J., Gómez-Gesteira, M., 2017. Towards
757 simulating floating offshore Oscillating Water Column converters with Smoothed Particle
758 Hydrodynamics. Coastal Engineering 126, 11-16.

759 Crespo, A.J.C., Hall, M., Domínguez, J.M., Altomare, C., Wu, M., Verbrugghe, T., Stratigaki, V., Troch, P.,
760 Gómez-Gesteira, M., 2018. Floating moored oscillating water column with meshless SPH method. In:
761 Proceedings of the 37th International Conference on Ocean, Offshore and Artic Engineering, Madrid,
762 Spain.

763 Davidson, J., Costello, R., 2020. Efficient Nonlinear Hydrodynamic Models for Wave Energy Converter Design
764 – A Scoping Study. Journal of Marine Science and Engineering 8, 35.

765 De Andrés, A.D., Guanche, R., Armesto, J.A., del Jesus, F., Vidal, C., Losada, I.J., 2013. Time domain model
766 for a two-body heave converter: Model and applications. Ocean Engineering 72, 116-123.

767 Designers' Guide to EN 1993-1-1 Eurocode 3: Design of Steel Structures. January 2005, 161-162

768 Domínguez, J.M., Altomare, C., Gonzalez-Cao, J., Lomonaco, P., 2019a. Towards a more complete tool for
769 coastal engineering: solitary wave generation, propagation and breaking in an SPH-based model. Coastal
770 Engineering Journal 61, 15-40.

771 Domínguez, J.M., Crespo, A.J.C., Hall, M., Altomare, C., Wu, M., Stratigaki, V., Troch, P., Cappietti, L.,
772 Gómez-Gesteira, M., 2019b. SPH simulation of floating structures with moorings. Coastal Engineering
773 153, 103560.

774 Drew, B., Plummer, A.R., Sahinkaya, M.N., 2009. A review of wave energy converter technology. In:
775 Proceedings of the Institution of Mechanical Engineers, Part A: Journal of Power and Energy 223, 887-
776 902

777 Eagleson, P., Dean, R., 1966. Small Amplitude Wave Theory. McGraw-Hill, New York.

778 Edge, B., Gamiel, K., Dalrymple, R.A., Herault, A., Bilotta, G., 2014. Application of gpusph to design of wave
779 energy. In: Proceedings of the 9th SPHERIC International Workshop, Paris, France.

780 Eriksson, M., Isberg, J., Leijon, M., 2005. Hydrodynamic modelling of a direct drive wave energy converter.
781 International Journal of Engineering Science 43, 1377-1387.

782 Evans, D., 1976. A theory for wave-power absorption by oscillating bodies. Journal of Fluid Mechanics 77(1),
783 1-25.

784 Falnes, J., 2002. Ocean Waves and Oscillating Systems. Cambridge University Press.

785 Folley, M., 2016. Numerical Modelling of Wave Energy Converters: State-of-the-Art Techniques for Single
786 Devices and Arrays. Elsevier.

787 Folley, M., Babarit, A., Child, B., Forehand, D., O'Boyle, L., Siverthorne, K., Spinneken, J., Stratigaki, V.,
788 Troch, P., 2012. A review of numerical modelling of wave energy converter arrays. In: 31st International
789 Conference on Ocean, Offshore and Arctic Engineering, American Society of Mechanical Engineers,
790 2012.

791 Fourtakas, G., Vacondio, R., Domínguez, J.M., Rogers, B.D., 2020. Improved density diffusion term for long
792 duration wave propagation. In: Proceedings of the International SPHERIC Workshop, Harbin, China.

793 González-Cao, J., Altomare, C., Crespo, A.J.C., Domínguez, J.M., Gómez-Gesteira, M., Kisacik, D., 2018. On
794 the accuracy of DualSPHysics to assess violent collisions with coastal structures. Computers & Fluids
795 179, 604-612.

796 Gotoh, H., Khayyer, A., 2018. On the state-of-the-art of particle methods for coastal and ocean engineering.
797 Coastal Engineering Journal 60, 79-103.

798 Hu, Z.Z., Greaves, D., Raby, A., 2016. Numerical wave tank study of extreme waves and wave-structure
799 interaction using OpenFoam. Ocean Engineering 126, 329-342

800 Jin, S., Patton, R.J., Guo, B., 2018. Viscosity effect on a point absorber wave energy converter hydrodynamics
801 validated by simulation and experiment. Renewable Energy 129 Part A, 500-512

802 Kamranzad, B., Hadadpour, S., 2020. A multi-criteria approach for selection of wave energy converter/location.
803 Energy 204, 117924.

804 Khayyer, A., Gotoh, H., Shimizu, Y., Gotoh, K., Falahaty, H., Shao, S., 2018. Development of a projection-
805 based SPH method for numerical wave flume with porous media of variable porosity. Coastal Engineering
806 140, 1-22.

807 Le Méhauté, B., 1976. An introduction to hydrodynamics and water waves. Springer

808 Lee, C.H., 1995. WAMIT theory manual. Massachusetts Institute of Technology, Department of Ocean
809 Engineering.

810 Li, Y., Yu, Y-H., 2012. A synthesis of numerical methods for modeling wave energy converter-point absorbers.
811 Renewable and Sustainable Energy Reviews 16(6), 4352-4364.

812 Ma, Q., 2010. Advances in Numerical Simulation of Nonlinear Water Waves. World Scientific.

813 Madsen, O.S., 1971. On the generation of long waves. Journal of Geophysical Research 76(36), 8672-8683.

814 Markel, P., Ringwood J., 2016. A review of wave-to-wire models for wave energy converters. Energies Energies
815 7(9), 506.

816 Monaghan, J.J., 1992. Smoothed particle hydrodynamics. Annual Review of Astronomy and Astrophysics 30,
817 543-574.

818 Monaghan, J.J., 2005. Smoothed particle hydrodynamics. Reports on Progress in Physics 68(8), 1703-1759.

819 Newman, J., 1976. The interaction of stationary vessels with regular waves. In: Proceedings of the 11th
820 Symposium on Naval Hydrodynamics, 759-794.

821 Newman, J.N., 2018. Marine hydrodynamics, MIT press.

822 Omidvar, P., Stansby, P.K. and Rogers, B.D., 2013. SPH for 3D floating bodies using variable mass particle
823 distribution. Int. J. Numer. Meth. Fluids 72, 427-452.

824 Penalba, M., Giorgi, G., Ringwood J.V., 2017. Mathematical modelling of wave energy converters: A review
825 of nonlinear approaches, Renewable and Sustainable Energy Reviews 78, 1188–1207.

826 Quon, E., Platt, A., Yu, Y-H., Lawson, M., 2016. Application of the most likely extreme response method for
827 wave energy converters. In: ASME 2016 35th International Conference on Ocean, Offshore and Arctic
828 Engineering. American Society of Mechanical Engineers Digital Collection

829 Rafiee, A., Elsaesser, B., Dias, F., 2013. Numerical simulation of wave interaction with an oscillating wave
830 surge converter. Proceedings ASME 32nd International Conference on Ocean, Offshore and Arctic
831 Engineering.

832 Rahmati, M.T., Aggidis, G.A., 2016. Numerical and experimental analysis of the power output of a point
833 absorber wave energy converter in irregular waves. Ocean Engineering 111, 483-492.

834 Ransley, E., Greaves, D., Raby, A., Simmonds, D., Jakobsen, M.M., Kramer, M., 2017. RANS-VOF modelling
835 of the Wavestar point absorber. Renewable Energy 109, 49-65.

836 Reabroy, R., Zheng, X., Zhang, L., Zang, J., Yuan, Z., Liu, M., Sun, K., Tiaple, Y., 2019. Hydrodynamic
837 response and power efficiency analysis of heaving wave energy converter integrated with breakwater.
838 Energy Conversion and Management 195, 1174-1186.

839 Ren, B., He, M., Dong, P., Wen, H., 2015. Nonlinear simulations of wave-induced motions of a freely floating
840 body using WCSPH method. Applied Ocean Research 50, 1–12.

841 Romano, A., Bellotti, G., Briganti, R., Franco, L., 2015. Uncertainties in the physical modelling of the wave
842 overtopping over a rubble mound breakwater: The role of the seeding number and of the test duration,
843 Coastal Engineering 103, 15-21.

844 Rota-Roselli, R.A., Vernengo, G., Altomare, C., Brizzolara, S., Bonfiglio, L., Guercio, R., 2018. Ensuring
845 numerical stability of wave propagation by tuning model parameters using genetic algorithms and
846 response surface methods. Environmental Modelling & Software 103, 62–73.

847 Tagliafierro, B., Crespo, A.J.C., Domínguez, J.M., García-Feal, O., Gómez-Gesteira, M., Canelas, R.B., Coe,
848 R.G., Bacelli, G., Cho, H., Spencer, S.J., Viccione, G., 2019. Numerical modelling of a point-absorbing
849 WEC model using DualSPHysics coupled with a multiphysics library. In: Proceedings of the 13th
850 European Wave and Tidal Energy Conference (EWTEC2019).

Tasora, A., Serban, R., Mazhar, H., Pazouki, A., Melanz, D., Fleischmann, J., Taylor, M., Sugiyama, H., Negrut, D., 2016. Chrono: An open source multi-physics dynamics engine. Lecture Notes in Computer Science. Springer International Publishing 19–49.

Tromans, P., Anaturk, A.R., Hagemeijer, P., 1991. A new model for the kinematics of large ocean waves-application as a design wave. In: Proceedings ISOPE-91 3.

Ursell, F., 1953. The long-wave paradox in the theory of gravity waves. Proceedings of the Cambridge Philosophical Society 49(4), 685-694.

Van Rij, J., Yu Y-H., Coe, R.G., 2018. Design load analysis for wave energy converters. In: ASME 2018 37th International Conference on Ocean, Offshore and Arctic Engineering. American Society of Mechanical Engineers Digital Collection.

Verbrugghe, T., Domínguez, J.M., Crespo, A.J.C., Altomare, C., Stratigaki, V., Troch, P., Kortenhaus, A., 2018. Coupling methodology for smoothed particle hydrodynamics modelling of non-linear wave-structure interactions. Coastal Engineering 138, 184-198.

Verbrugghe, T., Stratigaki, V., Altomare, C., Domínguez, J.M., Troch, P., Kortenhaus, A., 2019. Implementation of Open Boundaries within a Two-Way Coupled SPH Model to Simulate Nonlinear Wave–Structure Interactions. Energies 12(4), 697.

Violeau, D., Rogers, B. D., 2016. Smoothed particle hydrodynamics (SPH) for free-surface flows: past, present and future. Journal of Hydraulic Research 54(1), 1-26.

Weibull, W., 1951, A statistical distribution function of wide applicability, Journal of Applied Mechanics 18, 293-297.

Wendland, H., 1995. Piecewiese polynomial, positive definite and compactly supported radial functions of minimal degree. Advances in Computational Mathematics 4, 389-396.

Westphalen, J., Greaves, D.M., Williams, C.J.K., Hunt-Raby, A.C., Zang, J., 2012. Focused waves and wave–structure interaction in a numerical wave tank. Ocean Engineering 45, 9-21.

Westphalen, J., Greaves, M.D., Raby, A., Hu, Z.Z., Causon, D.M., Mingham, C.G., Omidvar, P., Stansby, P.K., Rogers, B.D., 2014. Investigation of wave-structure interaction using state of the art CFD techniques. Open Journal of Fluid Dynamics 4(1), 18-43.

Whittaker, C.N., Fitzgerald C.J., Raby A.C., Taylor P.H., Orszaghova J., Borthwick A.G.L., 2017. Optimisation of focused wave group runup on a plane beach. Coastal Engineering 121, 44.

Willmott, C.J., Ackleson, S.G., Davis, R.E., Feddema, J.J., Klink, K.M., Legates, D.R., O'Donnell, J., Rowe, C.M., 1985. Statistics for the evaluation of model performance. Journal of Geophysical Research 90(C5), 8995–9005.

Yeylaghi, S., Moa, B., Beatty, S., Buckham, B., Oshkai, P., Crawfoed, C., 2015. SPH Modeling of Hydrodynamic Loads on a Point Absorber Wave Energy Converter Hull. In: Proceedings of the 11th European Wave and Tidal Energy Conference (EWTEC2015).

Yu, Y-H., Lawson, M., Ruehl, K., Michelen, C., 2014. Development and demonstration of the WEC-Sim wave energy converter simulation tool. In: Proceedings of the 2nd Marine Energy Technology Symposium METS2014.

Yu, Y-H., Li, Y., 2013. Reynolds-averaged Navier-Stokes simulation of the heave performance of a two-body floating-point absorber wave energy system. Computers and Fluids 73, 104-114.

Zabala, I., Henriques J.C.C., Blanco, J.M., Gomez, A., Gato, L.M.C., Bidaguren, I., Falcao, A.F.O., Amezaga, A., Gomes, R.P.F., 2019. Wave-induced real-fluid effects in marine energy converters: Review and application to OWC devices. Renewable and Sustainable Energy Reviews 111, 535–549.

Zang, Z., Zhang, Q., Qi, Y., Fu, X., 2018. Hydrodynamic responses and efficiency analyses of heaving-buoy wave energy converter with PTO damping in regular and irregular waves. Renewable Energy 116, 527-542.